GEOPHYSICS, VOL. 79, NO. 4 (JULY-AUGUST 2014); P. T199–T217, 18 FIGS., 3 TABLES.
10.1190/GEO2013-0208.1

Numerical modeling of elastic-wave scattering by near-surface heterogeneities

Abdulaziz M. Almuhaidib[1] and M. Nafi Toksöz[2]

ABSTRACT

In land seismic data, scattering from surface and near-surface heterogeneities adds complexity to the recorded signal and masks weak primary reflections. To understand the effects of near-surface heterogeneities on seismic reflections, we simulated seismic-wave scattering from arbitrary-shaped, shallow, subsurface heterogeneities through the use of a perturbation method for elastic waves and finite-difference forward modeling. The near-surface scattered wavefield was modeled by looking at the difference between the calculated incident (i.e., in the absence of scatterers) and the total wavefields. Wave propagation was simulated for several earth models with different near-surface characteristics to isolate and quantify the influence of scattering on the quality of the seismic signal. The results indicated that the direct surface waves and the upgoing reflections were scattered by the near-surface heterogeneities. The scattering took place from body waves to surface waves and from surface waves to body waves. The scattered waves consisted mostly of body waves scattered to surface waves and were, generally, as large as, or larger than, the reflections. They often obscured weak primary reflections and could severely degrade the image quality. The results indicated that the scattered energy depended strongly on the properties of the shallow scatterers and increased with increasing impedance contrast, increasing size of the scatterers relative to the incident wavelength, decreasing depth of the scatterers, and increasing attenuation factor of the background medium. Also, sources deployed at depth generated weak surface waves, whereas deep receivers recorded weak surface and scattered body-to-surface waves. The analysis and quantified results helped in the understanding of the scattering mechanisms and, therefore, could lead to developing new acquisition and processing techniques to reduce the scattered surface wave and enhance the quality of the seismic image.

INTRODUCTION

In land seismic data acquisition, most of the seismic energy is scattered in the shallow subsurface layers by near-surface heterogeneities (e.g., wadis, large escarpments, dry river beds, and karst features) that are common in many arid regions such as the Arabian Peninsula and North Africa (Al-Husseini et al., 1981). When surface irregularities or volume heterogeneities are present (Figure 1), the data are contaminated with scattered surface-to-surface and body-to-surface waves (Levander, 1990), also known as scattered Rayleigh waves or ground roll. These unwanted coherent noise features can obscure weak body-wave reflections from deep structures. Direct surface-wave (Rayleigh-wave) scattering has been extensively studied in numerous previous studies (e.g., De Bremaecker, 1958; Knopoff and Gangi, 1960; Fuyuki and Matsumoto, 1980; Gélis et al., 2005). In exploration seismology, however, much less research has been done on the effects of near-surface heterogeneities on the upcoming reflections (Campman et al., 2005, 2006; Riyanti and Herman, 2005), especially in realistic cases of more complicated scatterers and background media. Therefore, the emphasis of this paper is more on the scattering of upcoming body waves.

Among all near-surface challenges, the signal-to-noise ratio (S/N) is most strongly affected by scattering and requires further investigation to obtain good seismic image quality. A field data example from Saudi Arabia (Figure 2) that was acquired in a desert environment shows the scattering phenomena. The scattered waves strongly affect the phase and amplitude of the recorded signal. They are usually neglected in most conventional imaging and interpretation schemes under simplified assumptions of the earth model

Manuscript received by the Editor 4 June 2013; revised manuscript received 26 January 2014; published online 27 May 2014.
[1]Formerly Massachusetts Institute of Technology, Earth Resources Laboratory, Cambridge, Massachusetts, USA; presently EXPEC Advanced Research Center, Saudi Aramco, Dhahran, Saudi Arabia. E-mail: muhaidib@alum.mit.edu.
[2]Massachusetts Institute of Technology, Earth Resources Laboratory, Cambridge, Massachusetts, USA. E-mail: toksoz@mit.edu.

(e.g., acoustic and single scattering). They can greatly affect subsequent processes such as migration, full-waveform inversion, and amplitude critical steps such as amplitude variation with offset. To explore means that could remove or reduce the effects of near-surface heterogeneities, it is helpful to determine what aspects of the heterogeneities contribute most to degradation of data quality. The scattering mechanisms can be studied by forward modeling to simulate the interactions between different wave phenomena caused by near-surface heterogeneities.

In this paper, we present a modeling approach for simulating the effects of elastic-wave scattering by near-surface heterogeneities. Several previous studies have formulated and examined solutions of the forward (Hudson, 1977; Wu and Aki, 1985; Beylkin and Burridge, 1990; Sato et al., 2012) and inverse (Blonk et al., 1995; Blonk and Herman, 1996; Ernst et al., 2002) elastic scattering problems for modeling and imaging based on the perturbation method and single-scattering (Born) approximation. These methods have limitations when dealing with large and high-contrast heterogeneities that violate the single-scattering (Born) approximation. Even though the finite-difference-injection method (Robertsson and Chapman, 2000) is more efficient, it cannot handle the interaction of the scattered wavefield with the free surface and bedrock layers (e.g., second- or high-order long-range interactions). Herman et al. (2000) and Campman et al. (2005, 2006) image and suppress near-receiver scattered surface waves assuming that scattering takes place immediately under the receivers. Other methods based on solving integral equations using the method of moments can take into account multiple scattering and can handle strong contrast and large heterogeneities (Riyanti and Herman, 2005; Campman and Riyanti, 2007). However, these methods are limited to laterally homogeneous embedding consisting of horizontal layers. These assumptions are not satisfied in areas with complex overburden, which makes these methods unsuitable for this problem. Numerical forward modeling of elastic waves, as opposed to analytical methods, plays a key role in this study. Because we solve the full wave equation based on finite difference, our modeling can handle more complicated background media, large contrasts in density and Lamé parameters, and irregular features, and it can generate synthetic seismograms that are accurate over a wide range of scatterer to wavelength ratios.

Finite-difference schemes have been used extensively for elastic-wave propagation (Kelly et al., 1976; Virieux, 1986; Levander, 1988; Graves, 1996). Treatments of the irregular free-surface boundary condition have also been developed and discussed in the literature (Fornberg, 1988; Tessmer et al., 1992; Hestholm and Ruud, 1994; Robertsson, 1996; Ohminato and Chouet, 1997; Zhang and Chen, 2006; Appelö and Petersson, 2009; AlMuhaidib et al., 2011). In this study, we use an accurate implementation of the standard staggered-grid (SSG) finite-difference scheme (Virieux, 1986; Levander, 1988; Zhang, 2010) with the convolution perfectly matched layer absorbing boundary condition (Komatitsch and Martin, 2007; Martin and Komatitsch, 2009; Zhang and Shen, 2010) to fully model elastic waves in the presence of heterogeneity. The internal interfaces are represented by the so-called effective medium parameters (Moczo et al., 2002) to avoid spurious numerical diffractions caused by sharp material discontinuity due to the spatial grid. The density is calculated by arithmetic average, and the Lamé parameters are calculated by harmonic average. The SSG scheme is fourth-order accurate in space (including the free-surface boundary) and second-order accurate in time. The free-surface boundary is treated by adjusting the finite-difference approximations to the z-derivative close to the surface (Kristek et al., 2002), which provides fourth-order accuracy in space and minimizes numerical dispersion.

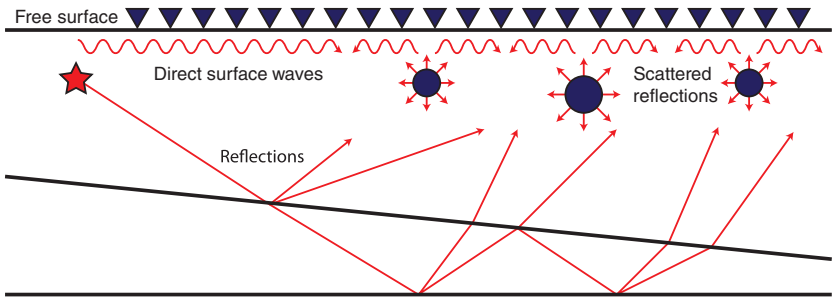

Figure 1. Schematic earth model showing how most of the seismic energy is scattered in the shallow subsurface layers.

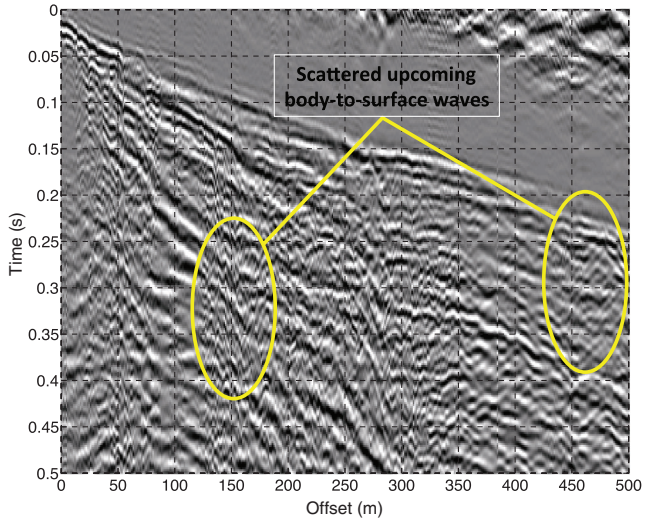

Figure 2. Field data from Saudi Arabia showing upcoming body-wave scattering to surface waves caused by near-surface complexities.

We compute numerical simulations in two dimensions for simple earth models with near-surface scatterers. We consider irregular interface and finite scatterers with contrasts in density and Lamé parameters that are embedded in the shallow subsurface to analyze and assess the effects of near-surface scattering mechanisms on recorded seismic waveforms. The perturbation method for elastic waves is used to separate the scattered wavefield from the total wavefield based on a perturbation of the wave equation with respect to medium parameters. The method decomposes the medium parameters into background and perturbation parts, and it allows us to model scattering from arbitrary shape scatterers and the interaction of the multiply scattered wavefield with the free surface. Modeling elastic seismic data through (1) a baseline model (i.e., background) and (2) a monitor model (i.e., background plus perturbation) is very common in the context of 4D seismic monitoring

studies (Greaves and Fulp, 1987; Pullin et al., 1987; Lumley, 1995). However, the focus of this study is different because we are looking at the elastic-wave scattering phenomena due to near-surface heterogeneities instead of reflected phase and amplitude changes due to time-variant changes in reservoir conditions. In this study, we carry out extensive calculations to study the effects of the acquisition geometry (e.g., source and receiver depths), the quality factor of the background medium, and the elastic properties of shallow subsurface scatterers (e.g., size, depth, and impedance contrast) on the near-surface scattered wavefield.

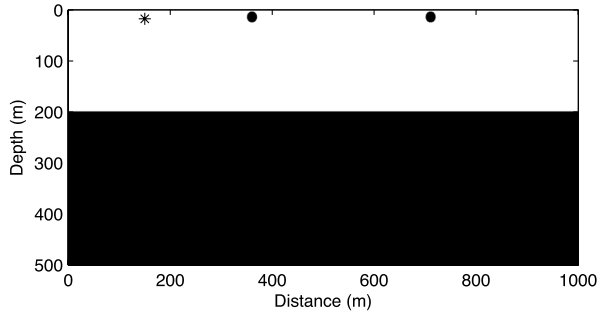

Figure 3. Synthetic earth model — a single layer over half a space with two circular scatterers embedded in the shallow layer. The two scatterers are located at $(x, z) = (360\text{ m}, 15\text{ m})$ and $(x, z) = (720\text{ m}, 15\text{ m})$, each has a 20-m diameter and an impedance contrast corresponding to 0.36. The P-wave, S-wave, and density values of the first layer are 1800 m/s, 1000 m/s, and 1750 kg/m^3, and for the half-space and scatterers, they are 3000 m/s, 1500 m/s, and 2250 kg/m^3, respectively. The source is located at $(x, z) = (150\text{ m}, 10\text{ m})$ as indicated by the red star. The receivers are located on the surface with 50-m near-offset and 5-m space intervals.

MODELING OF ELASTIC-WAVE PROPAGATION AND SCATTERING WITH NEAR-SURFACE HETEROGENEITIES

In this section, we present the mathematical approach to explain elastic-wave scattering using the perturbation method. The general wave equation for the elastic isotropic medium is

$$\rho\ddot{\mathbf{u}} - (\lambda + 2\mu)\nabla(\nabla \cdot \mathbf{u}) + \mu\nabla \times (\nabla \times \mathbf{u}) = \mathbf{f}, \qquad (1)$$

where $\mathbf{u}$ is the displacement vector wavefield, $\mathbf{f}$ is the body force term, and the medium is described by three parameters: the Lamé constants $\lambda(x)$ and $\mu(x)$, and density $\rho(x)$. Seismic P- and S-wave velocities are $c_p = \sqrt{(\lambda + 2\mu)/\rho}$ and $c_s = \sqrt{\mu/\rho}$. The perturbation theory decomposes the medium parameters into background and perturbation parts

$$\begin{aligned} \rho(x) &= \rho_0 + \delta\rho(x), \\ \lambda(x) &= \lambda_0 + \delta\lambda(x), \\ \mu(x) &= \mu_0 + \delta\mu(x). \end{aligned} \qquad (2)$$

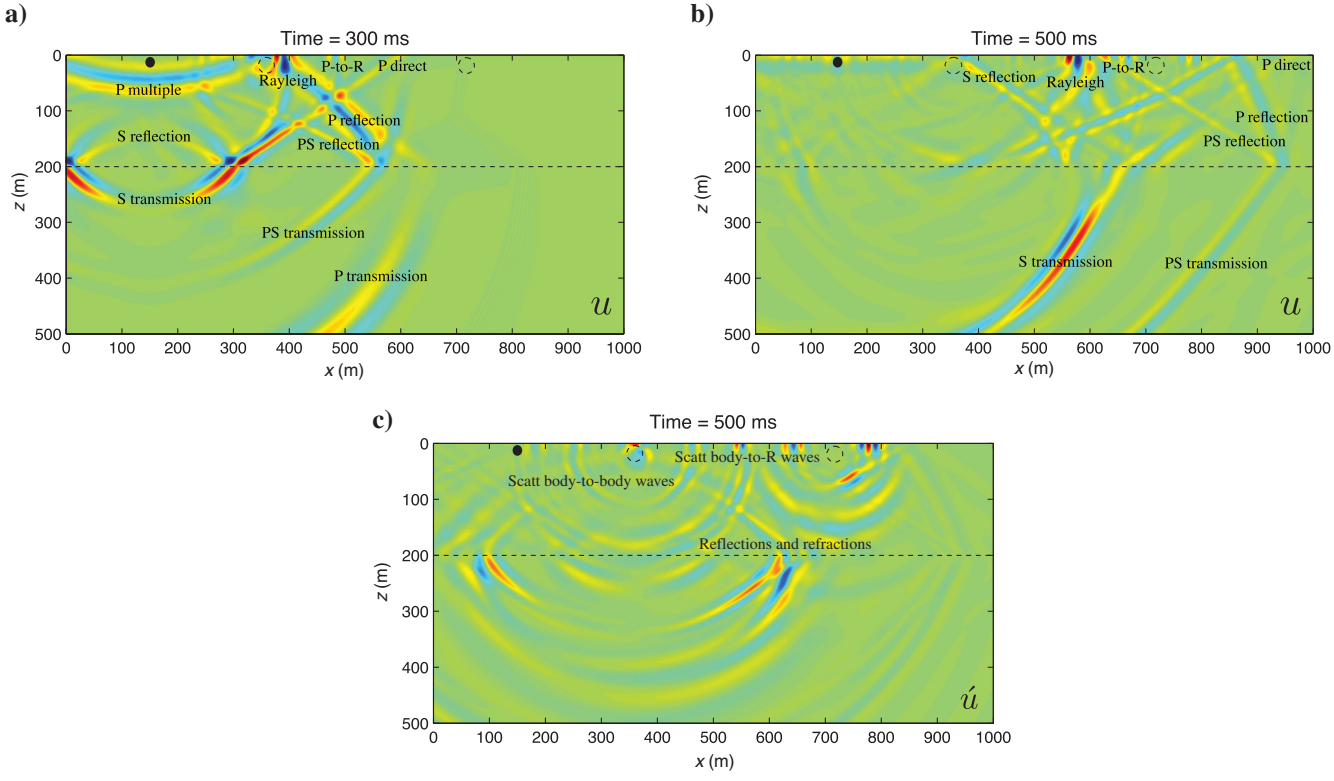

Figure 4. Snapshots of the total (u) and scattered (u') wavefields for the model in Figure 3: (a) the total field at 300 ms, (b) total field at 500 ms, and (c) the scattered field at 500 ms. The source of scattering is reflected or refracted body waves. The scatterers excite primary, shear, and also surface waves due to the proximity to the free surface. The source is located at $(x, z) = (150\text{ m}, 10\text{ m})$ and indicated by the black circle. The reflector is indicated by the dashed line at 200 m depth. Note that we do not show the scattered surface-to-surface waves in the scattered wavefield because it is much larger in amplitude compared to the scattered body-to-surface waves.

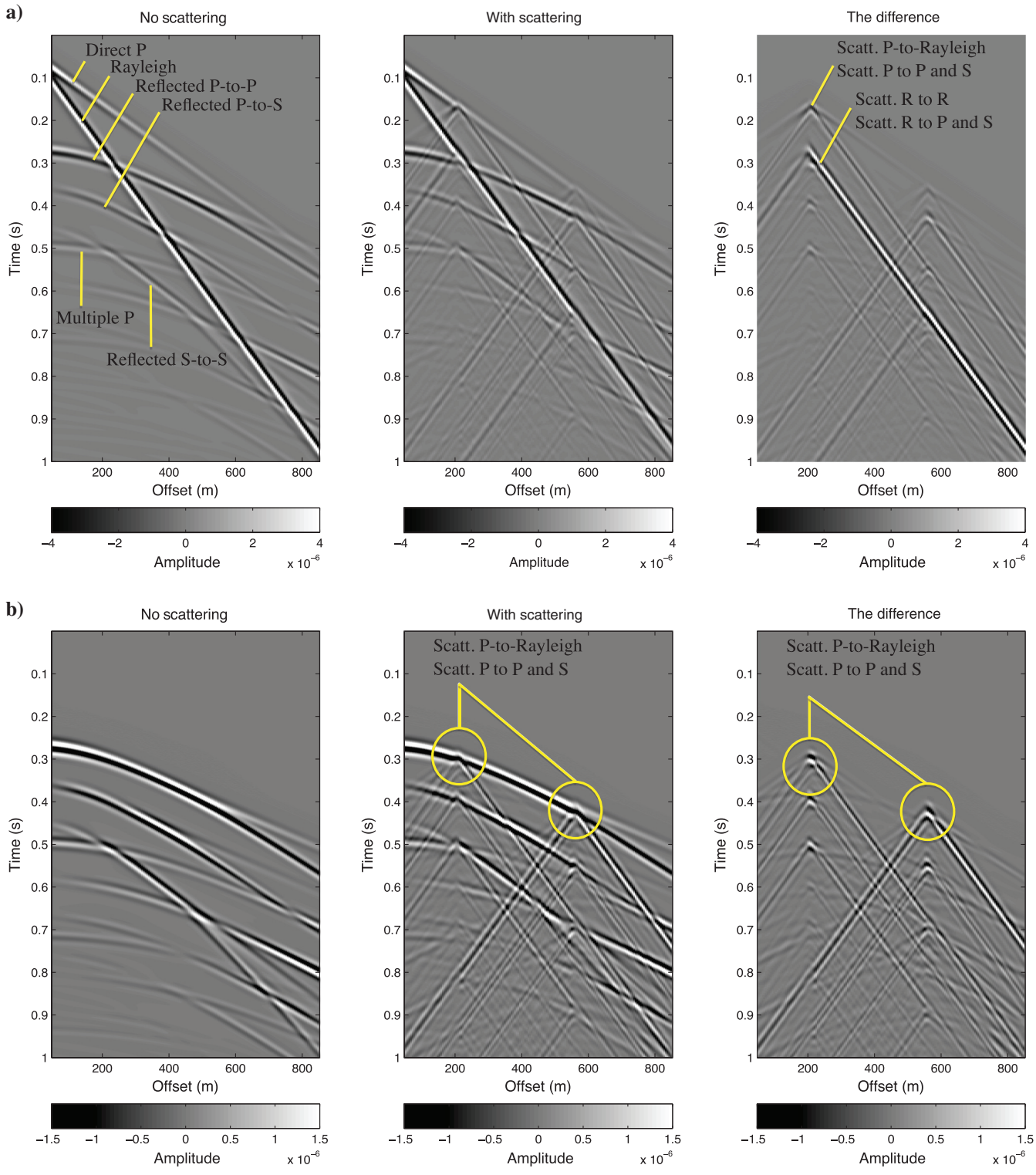

Figure 5. Finite-difference simulations (v_z-component) showing the scattering effects due to near-surface heterogeneities for the model in Figure 3 (a) shows the results including the direct surface wave and (b) with the direct surface wave removed: (left) incident wavefield simulated using the model without scatterers, (middle) total wavefield simulated using the model with scatterers, and (right) scattered wavefield (i.e., the difference between the total and incident wavefields). An explosive point source with a 30-Hz Ricker wavelet is used. The source is located at 10-m depth, and the receivers are located on the surface. Note the complexity due to scattering of the reflected arrivals. (Scatt and R indicate scattered and Rayleigh waves, respectively.)

We denote by δ and subscript 0 the perturbed and background (reference) medium parameters, respectively. The wavefield in the background medium is $\mathbf{u}_0$, and it satisfies the elastic-wave equation

$$\rho_0\ddot{\mathbf{u}}_0 - (\lambda_0 + 2\mu_0)\nabla(\nabla \cdot \mathbf{u}_0) + \mu_0\nabla \times (\nabla \times \mathbf{u}_0) = \mathbf{f}. \quad (3)$$

We consider the total wavefield $\mathbf{u}$ in the heterogeneous medium as two parts: the incident wavefield $\mathbf{u}_0$ in the background medium,

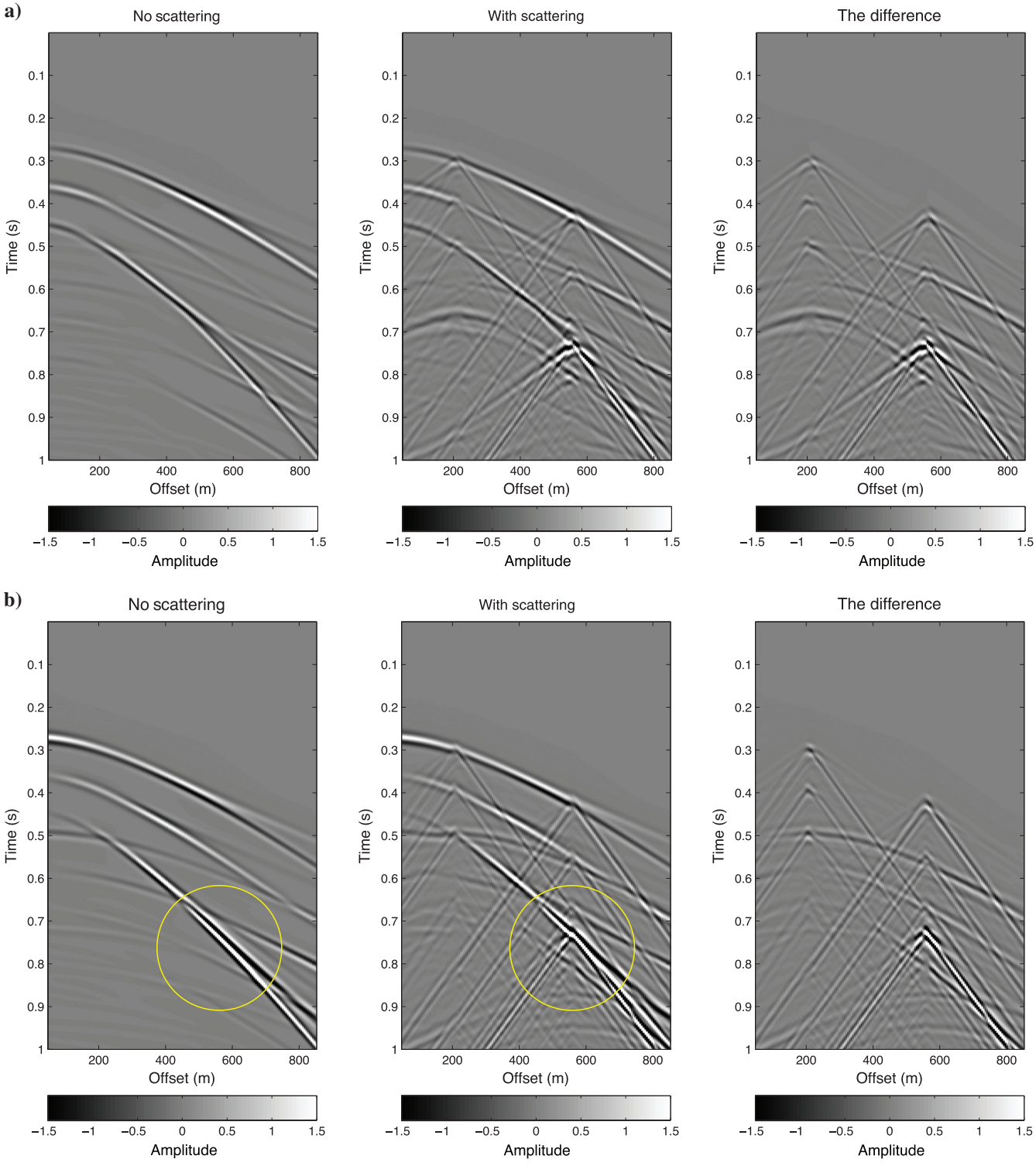

Figure 6. Simulated waveforms for the model in Figure 3 with vertical source and receivers on the surface: (a) v_x-component and (b) v_z-component. The incident, total, and scattered wavefields are shown from left to right, respectively. Note that the direct surface wave is removed. Also note the strong amplitudes of the shear-wave reflection and refraction as indicated by the yellow circles at mid- and far-offset traces (of the v_z-component) due to the radiation pattern of the vertical source.

which is the wavefield in the absence of scatterers, and the scattered wavefield $\mathbf{u}'$, which is the difference between the total and incident wavefields,

$$\mathbf{u}' = \mathbf{u} - \mathbf{u}_0. \tag{4}$$

The definition of the perturbation quantities leads to the derivation of a wave equation for the scattered wavefield $\mathbf{u}'$. By subtracting equation 3 from 1, we obtain

$$\rho_0 \ddot{\mathbf{u}}' - (\lambda_0 + 2\mu_0)\nabla(\nabla \cdot \mathbf{u}') + \mu_0 \nabla \times (\nabla \times \mathbf{u}') = -[\delta\rho \ddot{\mathbf{u}} - (\delta\lambda + 2\delta\mu)\nabla(\nabla \cdot \mathbf{u}) + \delta\mu \nabla \times (\nabla \times \mathbf{u})]. \tag{5}$$

The left side of equation 5 describes wavefield scattering in the background medium (i.e., reference medium parameters) that includes multiple scattering waves (the derivation is given in Appendix A). The right side is equivalent to an elastic source term that depends on the perturbations of the medium parameters and the Green's function of the heterogeneous medium. Solving for the scattered wavefield $\mathbf{u}'$ can be achieved by either solving equation 5 directly based on the perturbation method (Wu, 1989) or by solving equations 1 and 3 independently and then subtracting the incident from the total wavefield. In this paper, we follow the latter approach.

For numerical modeling, we use a 2D Cartesian system with the horizontal positive x-axis pointing to the right and the positive vertical z-axis pointing down. The basic governing equations (i.e., the system of first-order partial differential equations) that describe elastic-wave propagation in the velocity-stress formulation (Virieux, 1986) are

$$\rho \frac{\partial v_x}{\partial t} = \frac{\partial \sigma_{xx}}{\partial x} + \frac{\partial \sigma_{xz}}{\partial z},$$
$$\rho \frac{\partial v_z}{\partial t} = \frac{\partial \sigma_{zx}}{\partial x} + \frac{\partial \sigma_{zz}}{\partial z}. \tag{6}$$

The constitutive laws for an isotropic medium are

$$\frac{\partial \sigma_{xx}}{\partial t} = (\lambda + 2\mu)\frac{\partial v_x}{\partial x} + \lambda \frac{\partial v_z}{\partial z},$$
$$\frac{\partial \sigma_{zz}}{\partial t} = (\lambda + 2\mu)\frac{\partial v_z}{\partial z} + \lambda \frac{\partial v_x}{\partial x},$$
$$\frac{\partial \sigma_{xz}}{\partial t} = \mu\left(\frac{\partial v_x}{\partial z} + \frac{\partial v_z}{\partial x}\right), \tag{7}$$

where v_x and v_z are the velocity components, σ_{ij} are the stresses, λ and μ are the Lamé parameters, and ρ is the density. The system of equations 6 and 7 is discretized and solved numerically using finite-difference schemes. The finite-difference scheme used in the numerical simulation can also handle viscoelastic materials by using the Emmerich and Korn (1987) model to include attenuation defined by Q values. We assume Q is constant with frequency.

Table 1. Summary of all the cases studied and their corresponding figure numbers.

Figure	Varying model parameter
7	Source frequency
8	Source depth
9	Receiver depth
11	Contrast of scatterers
12	Size of scatterers
13	Depth of scatterers
14	Quality factor
18	Interface scattering

APPLICATIONS TO THE EARTH MODEL WITH NEAR-SURFACE HETEROGENEITIES

To study the effects of near-surface heterogeneities on the recorded waveforms, we consider a simple earth model with a single layer over half a space and two circular scatterers embedded in the shallow layer (Figure 3). The two scatterers are located at $(x, z) = (360\text{ m}, 15\text{ m})$ and $(x, z) = (720\text{ m}, 15\text{ m})$, each has a 20-m diameter and an impedance contrast corresponding to 0.36. The P-wave, S-wave, and density values of the first layer are 1800 m/s, 1000 m/s, and 1750 kg/m^3, and for the half-space and scatterers, they are 3000 m/s, 1500 m/s, and 2250 kg/m^3, respectively. The domain has $N_x = 1001$ and $N_z = 501$ grid points with 1-m grid spacing (i.e., Δx and Δz), that is, 500-m depth (along the z-axis) and 1000 m distance (along the x-axis). The time step is 0.2 ms. An explosive point source is used with a Ricker wavelet and 30-Hz dominant frequency (~75-Hz maximum frequency). The source is located at $(x, z) = (150\text{ m}, 10\text{ m})$. The receivers are located on the surface with 50-m near-offset and 5-m space intervals. In this paper, we consider only the vertical component of the particle velocity field (v_z). The scatterers are treated in the numerical scheme as a density and velocity perturbation. The grid size of the model is small enough to capture the shape of the scatterers. To avoid spurious numerical diffractions caused by material discontinuity due to the spatial grid, arithmetic, and harmonic averages (smoothing) (Moczo et al., 2002) are applied to the density and elastic constants at each grid point.

Table 2. Material properties for models with different contrasts. The impedance contrasts are calculated for different material properties relative to layer 1.

	V_P (m/s)	V_S (m/s)	Density (kg/m^3)	Impedance contrast
Layer I	1800	1000	1750	—
Layer II	3000	1500	2250	0.36
Scatterers a	2400	1200	1800	0.16
Scatterers b	2700	1350	2025	0.27
Scatterers c	3000	1500	2250	0.36

Snapshots of the total and scattered wavefields that are governed by equations 1 and 5, respectively, are shown in Figure 4. Note that in this figure, we do not show the scattered surface-to-surface waves in the scattered wavefield because they are much larger in amplitude compared to the scattered body-to-surface waves. Removal of the direct surface waves is achieved by first computing the wavefield

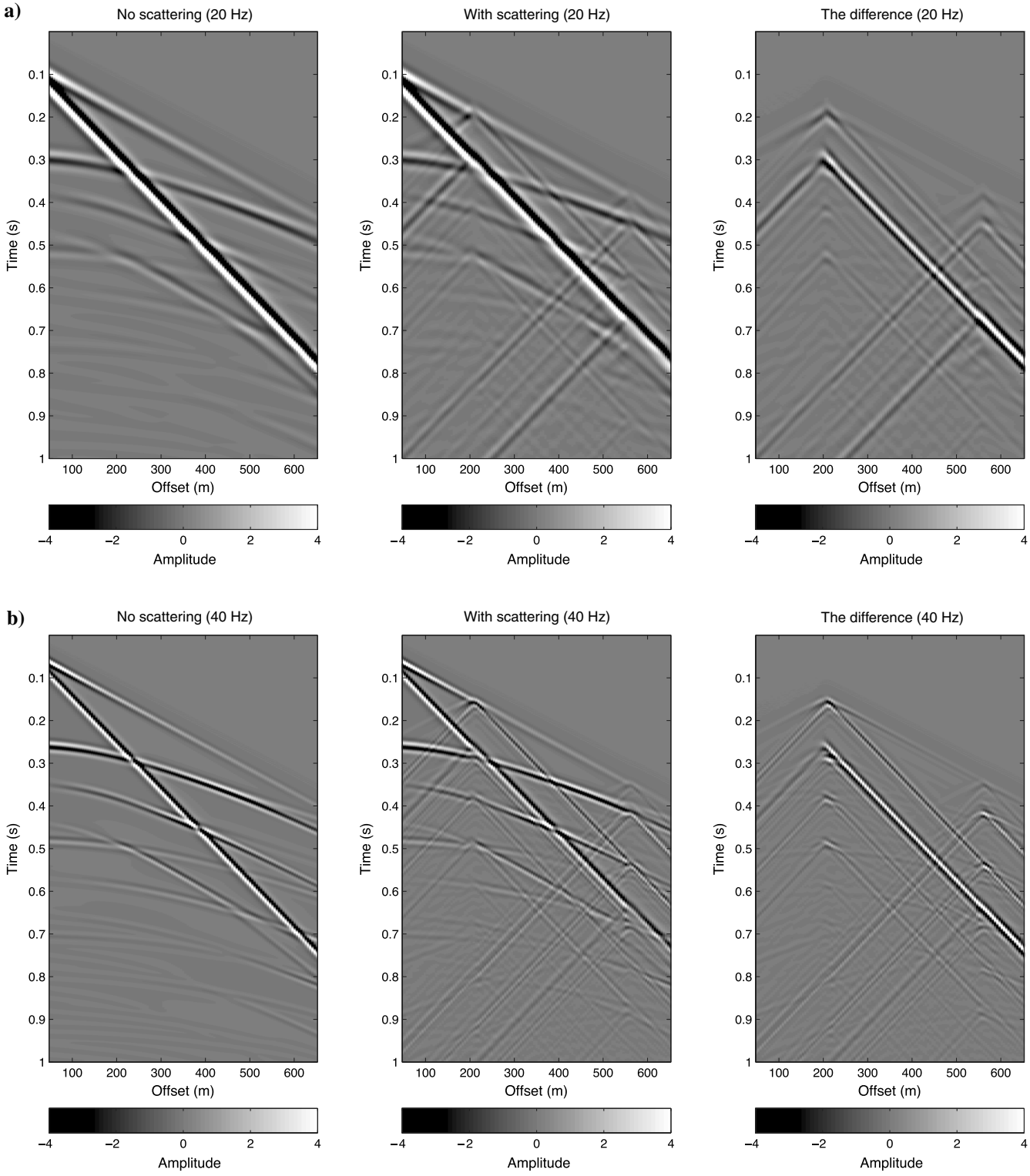

Figure 7. Simulated waveforms (v_z-component) for the model in Figure 3 An explosive point source is used with (a) 20-Hz and (b) 40-Hz dominant frequencies. The incident, total, and scattered wavefields are shown from left to right, respectively.

for a homogeneous full space with and without the scatterers. Then, we subtract the direct surface waves from the incident and total wavefields to look only at scattered body waves. The upcoming body P- and S-wave reflections, including multiples, impinge on the near-surface heterogeneities and scatter to weak P- and S-waves, acting as secondary sources. Because the scatterers, which are at

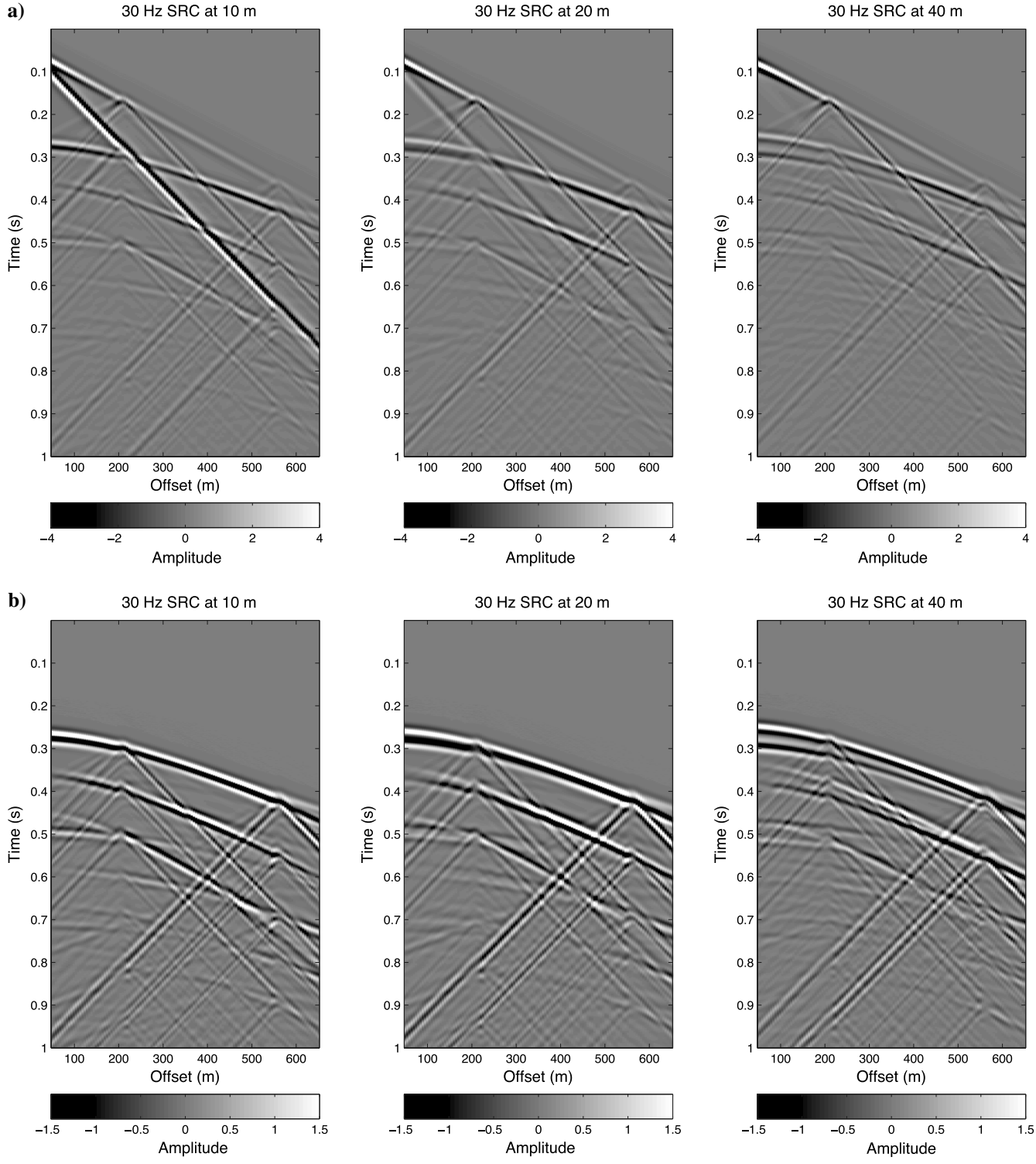

Figure 8. Finite-difference simulations (v_z-component) for the scattering model with different source depths (10, 20, and 40 m from left to right): (a) including the direct surface wave and (b) with the direct surface wave removed. An explosive point source with a 30-Hz Ricker wavelet is used. The receivers are located on the surface.

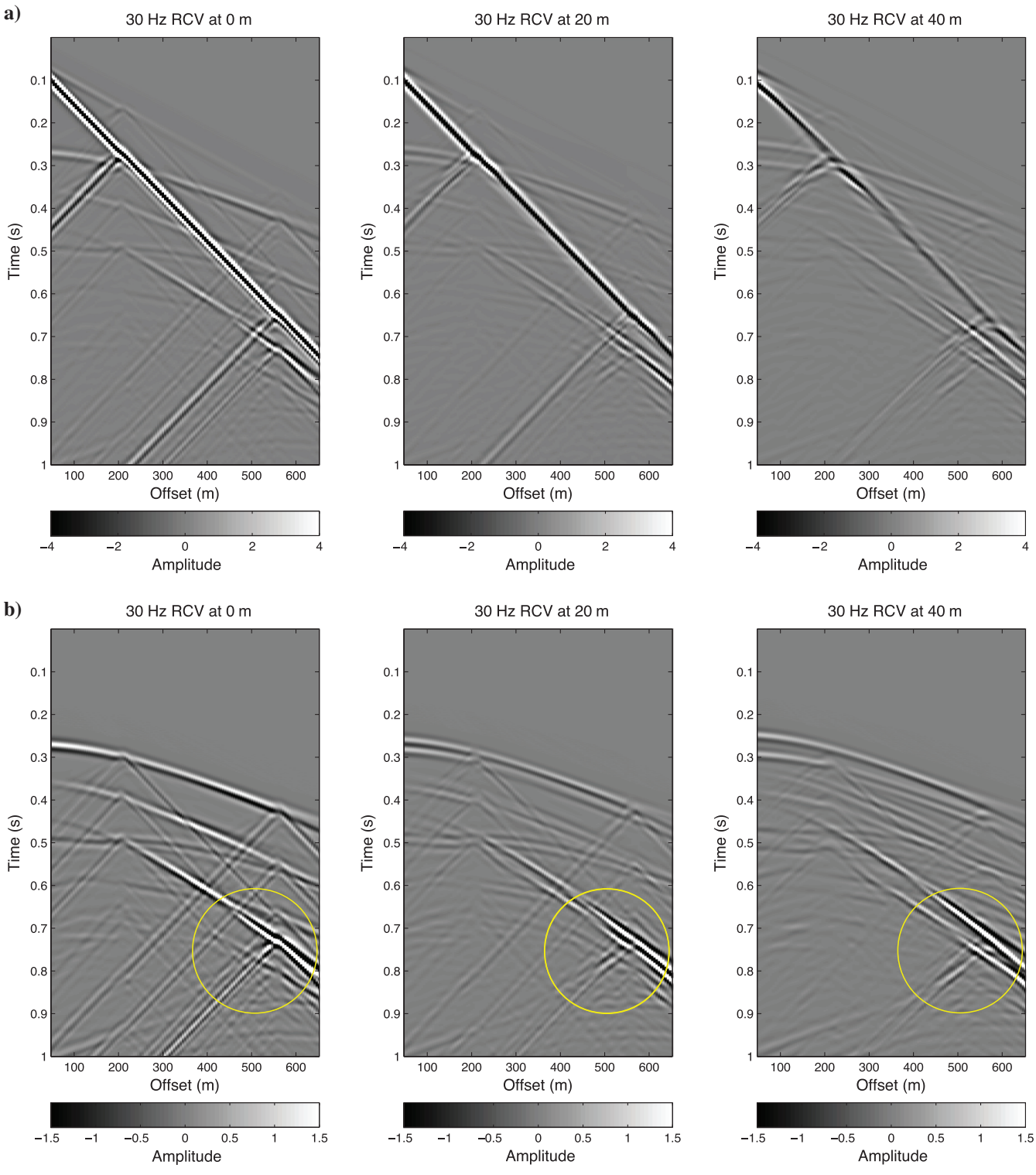

Figure 9. Finite-difference simulations (v_z-component) for the scattering model with different receiver depths (0, 20, and 40 m from left to right): (a) including the direct surface wave and (b) with the direct surface wave removed. A vertical source with a 30-Hz Ricker wavelet is located at the surface. Note the strong amplitudes of the shear-wave reflection and refraction as indicated by the yellow circles at mid- and far-offset traces due to the radiation pattern of the vertical source. At 40-m receiver depth, most of scattered waves appear to be body waves. Note also that the reflections are not as prominent as they are for surface receivers. At the surface, the amplitude doubles. At depth, upgoing and downgoing waves interfere.

15-m depth, are shallower than one-third of the wavelength ($\lambda_p = 60$ m), the body-wave reflections (incident wavefield) scatter to strong surface waves. These wave features are also shown in the shot gathers in Figure 5. The scattered surface waves are comparable in amplitude to the reflected signal. A few of these scatterers that are close to the free surface could mask the primary reflections by the scattered body-to-surface waves.

We also model a vertical source placed at the surface, which represents a more realistic vibrator-type field acquisition (Figure 6). We observe strong amplitudes of the shear-wave reflection and refraction at mid- and far-offset traces due to the radiation pattern of the vertical source. In all the cases we study in this paper (except for the source and receiver depth analysis), we consider an explosive point source at 10-m depth to minimize surface-wave energy relative to body-wave reflections (see the figure summary in Table 1).

Effect of source frequency and source and receiver depths

The seismic source frequency and source and receiver depths have significant impact on the recorded waveforms, especially on the strength of the surface-wave energy. To examine the effects of these factors, we simulate synthetic seismograms for the earth model in Figure 3 with different source frequencies (20, 30, and 40 Hz), source depths (10, 20, and 40 m), and receiver depths (0, 20, and 40 m), as shown in Figures 7–9, respectively.

The excitation of surface waves depends on the source depth and frequency. Direct surface-wave energy decreases with increasing source depth and increasing frequency at a given depth. At a depth of 10 m, sources with 20-Hz frequency ($\lambda_p = 90$ m) excite stronger surface waves (Figure 7) than those with 40-Hz frequency ($\lambda_p = 45$ m). For sources with 30-Hz dominant

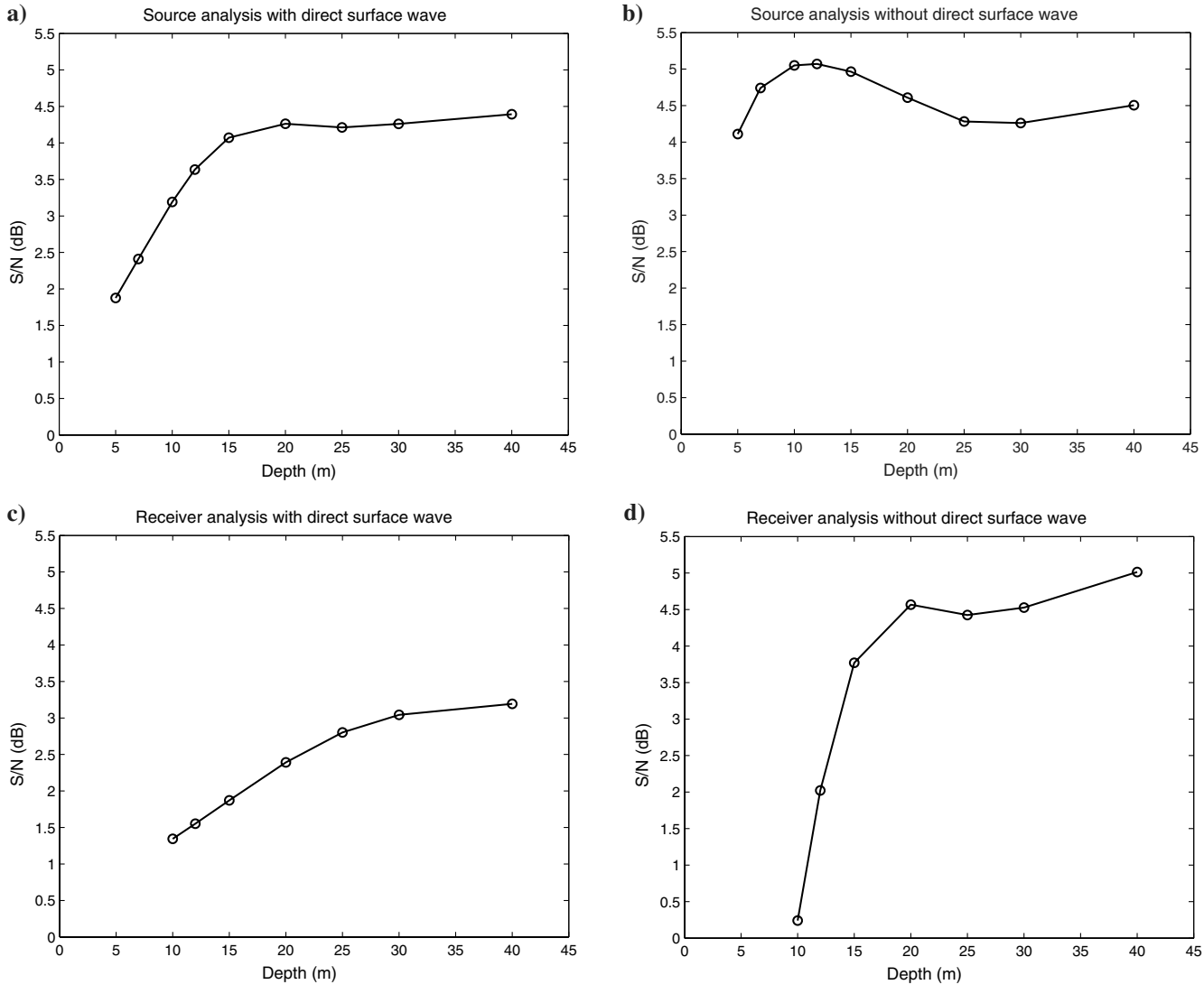

Figure 10. The effects of source and receiver depths on the S/N due to near-surface heterogeneities: (a and b) source analysis and (c and d) receiver analysis. Note that sources at deeper depths generate less surface-wave energy and therefore improve the S/N as shown in (a), but the source depth has no effect on the scattered body-to-surface waves as shown in (b). Receivers at deeper depths, however, improve the S/N in both cases: (c) the surface waves and (d) scattered body waves to surface waves.

frequency ($\lambda_p = 60$ m), the excited surface-wave energy is strong for shallow sources at 10-m depth (Figure 8), whereas it is much weaker for deeper sources at 40 m ($>\lambda_p/3$).

To quantitatively assess the influence of near-surface heterogeneities, we assume that scattered waves are noise and calculate the S/N in decibels (dB):

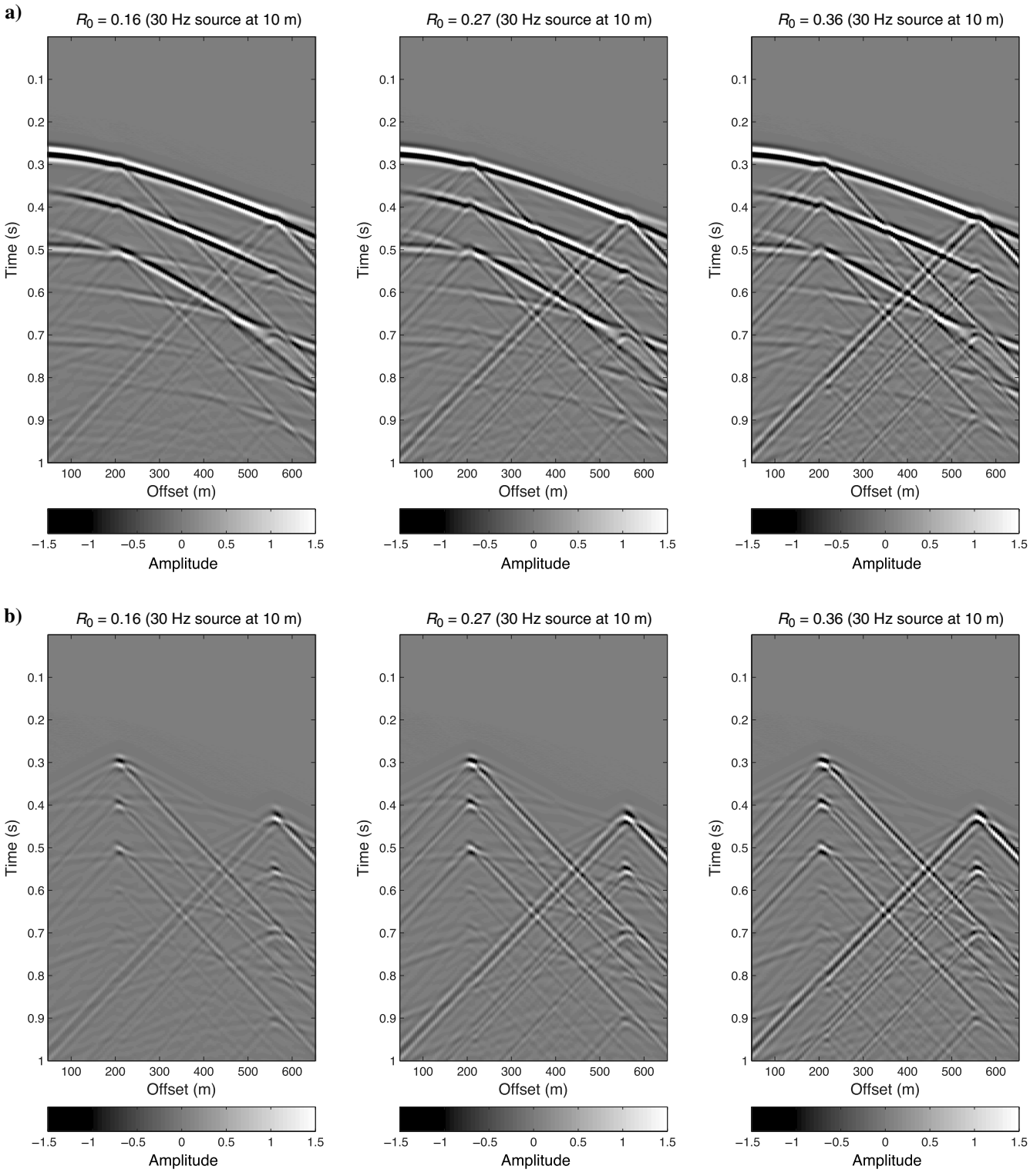

Figure 11. Simulated waveforms (v_z-component) for the scattering model with different impedance contrasts (0.16, 0.27, and 0.36) from left to right. The source (30 Hz) is located at 10-m depth, and the receivers are located on the surface: (a) the total wavefield simulated using the model with scatterers and (b) the scattered wavefield (i.e., the difference between the total and incident wavefields).

$$\mathrm{S/N(dB)} = 10\log_{10}\frac{\sum_{i=1}^{N}\sum_{j=1}^{M} u_0(i,j)^2}{\sum_{i=1}^{N}\sum_{j=1}^{M}\left(u(i,j)-u_0(i,j)\right)^2}, \quad (8)$$

where $u_0(i,j)$ are the sample values considered to be unaffected by noise (i.e., the incident wavefield propagated using the model with homogeneous near-surface layers), $u(i,j)$ are the data affected by

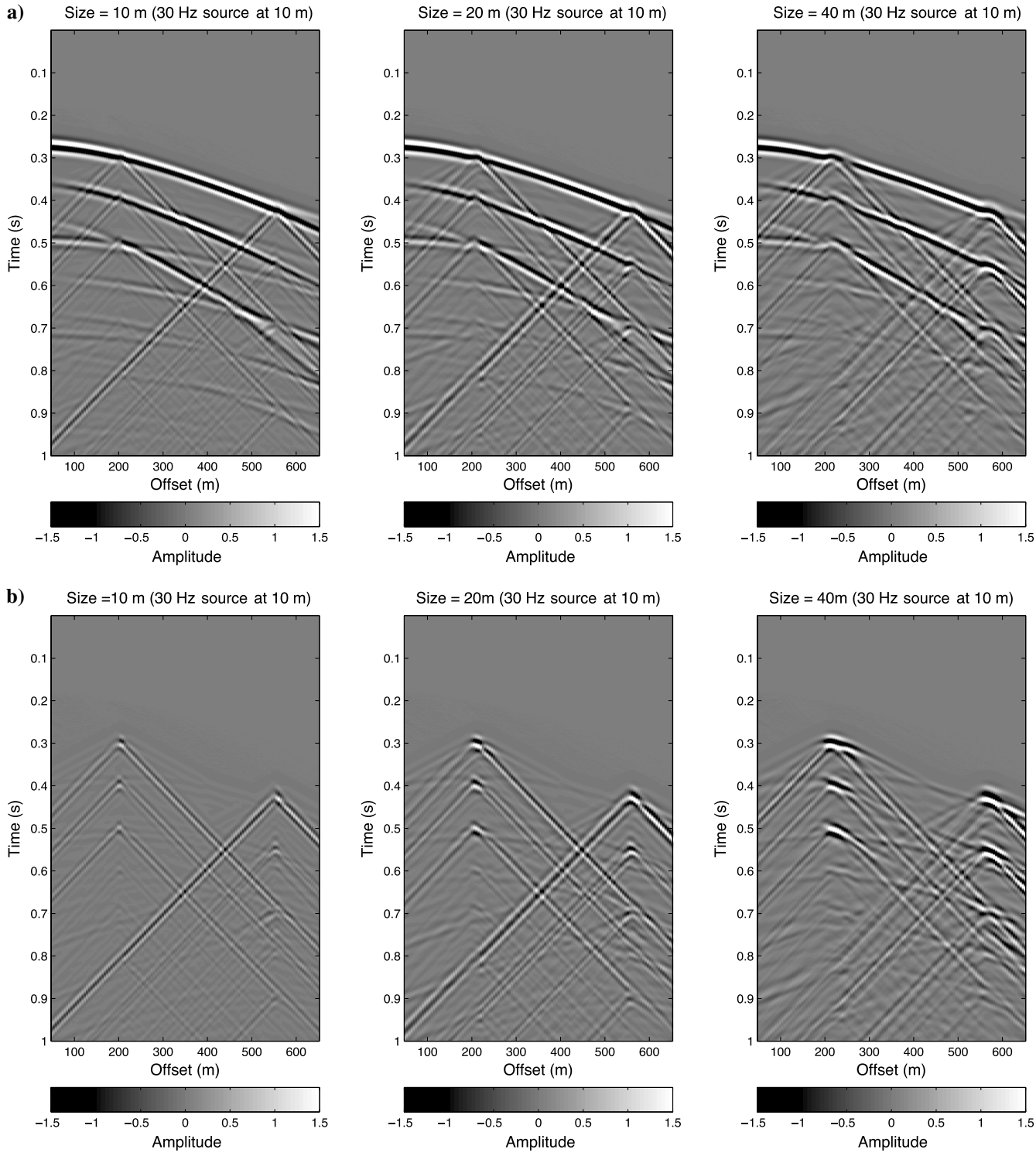

Figure 12. Simulated waveforms (v_z-component) for the scattering model with different scatterer sizes (10-, 20-, and 40-m diameter) from left to right, with the center of the scatterers at 10-, 15-, and 25-m depth, respectively. The top of the scatterers is at a 5-m depth below the free surface. The source (30 Hz) is located at a 10-m depth, and the receivers are located on the surface: (a) the total wavefield simulated using the model with scatterers and (b) the scattered wavefield (i.e., the difference between the total and incident wavefields).

noise (i.e., the total wavefield propagated using the model with near-surface heterogeneity), and M and N are the number of traces and time samples, respectively.

We study the effects of source and receiver depths on the S/N due to near-surface heterogeneities. The synthetic seismograms as functions of source and receiver depths are shown in Figures 8 and 9.

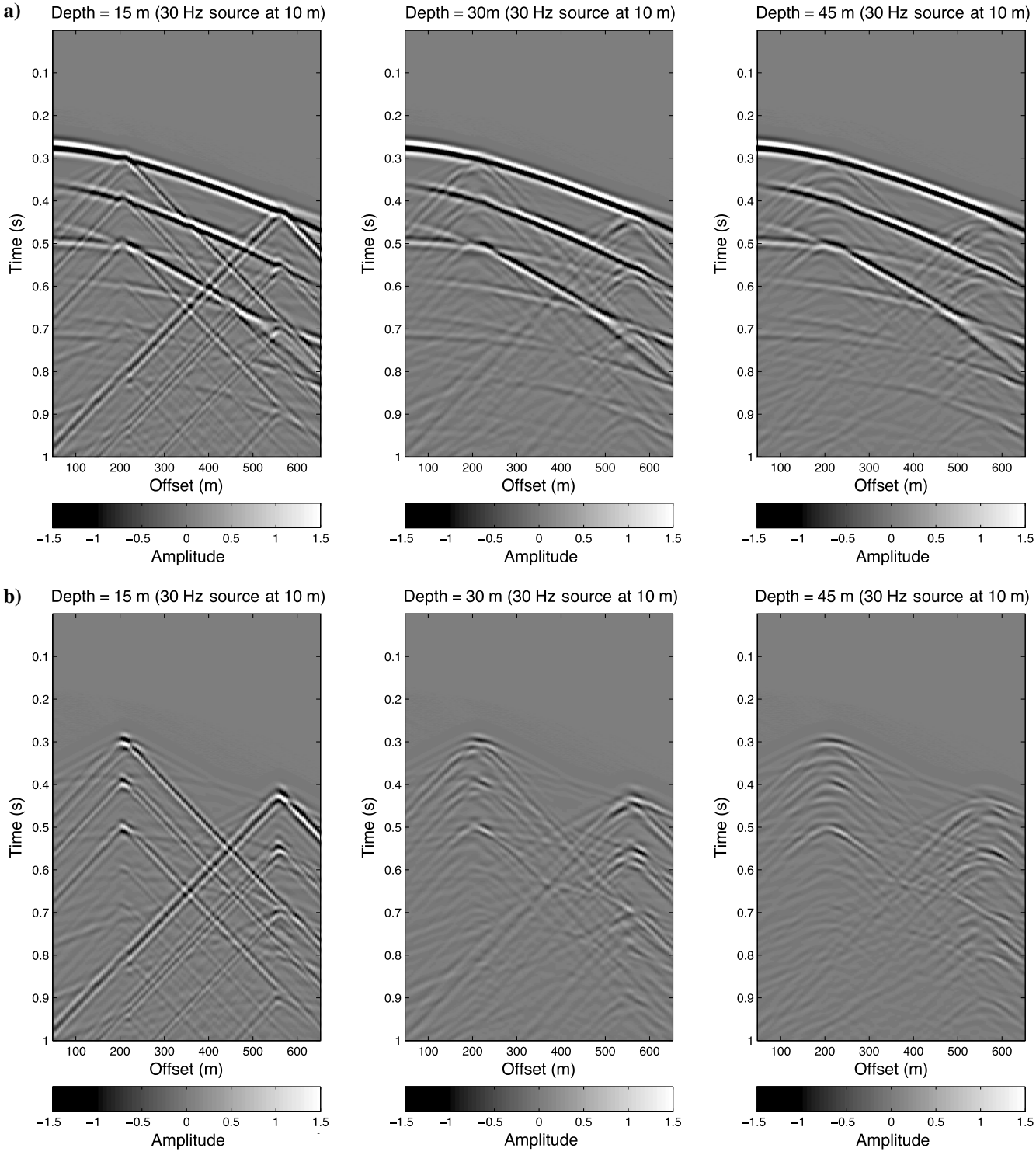

Figure 13. Simulated waveforms (v_z-component) for the scattering model with different scatterer depths (15, 30, and 45 m) from left to right. The source (30 Hz) is located at 10-m depth and the receivers are located on the surface: (a) the total wavefield simulated using the model with scatterers and (b) the scattered wavefield (i.e., the difference between the total and incident wavefields).

The corresponding S/Ns are shown in Figure 10. Seismic sources deployed at depth can minimize the amount of propagating direct surface-wave energy and, therefore, improve the S/N in the seismic records as the amplitude of surface waves decays exponentially with depth (Figure 10a). However, source depths have no effects on the scattered body-to-surface waves, mainly because scattered waves

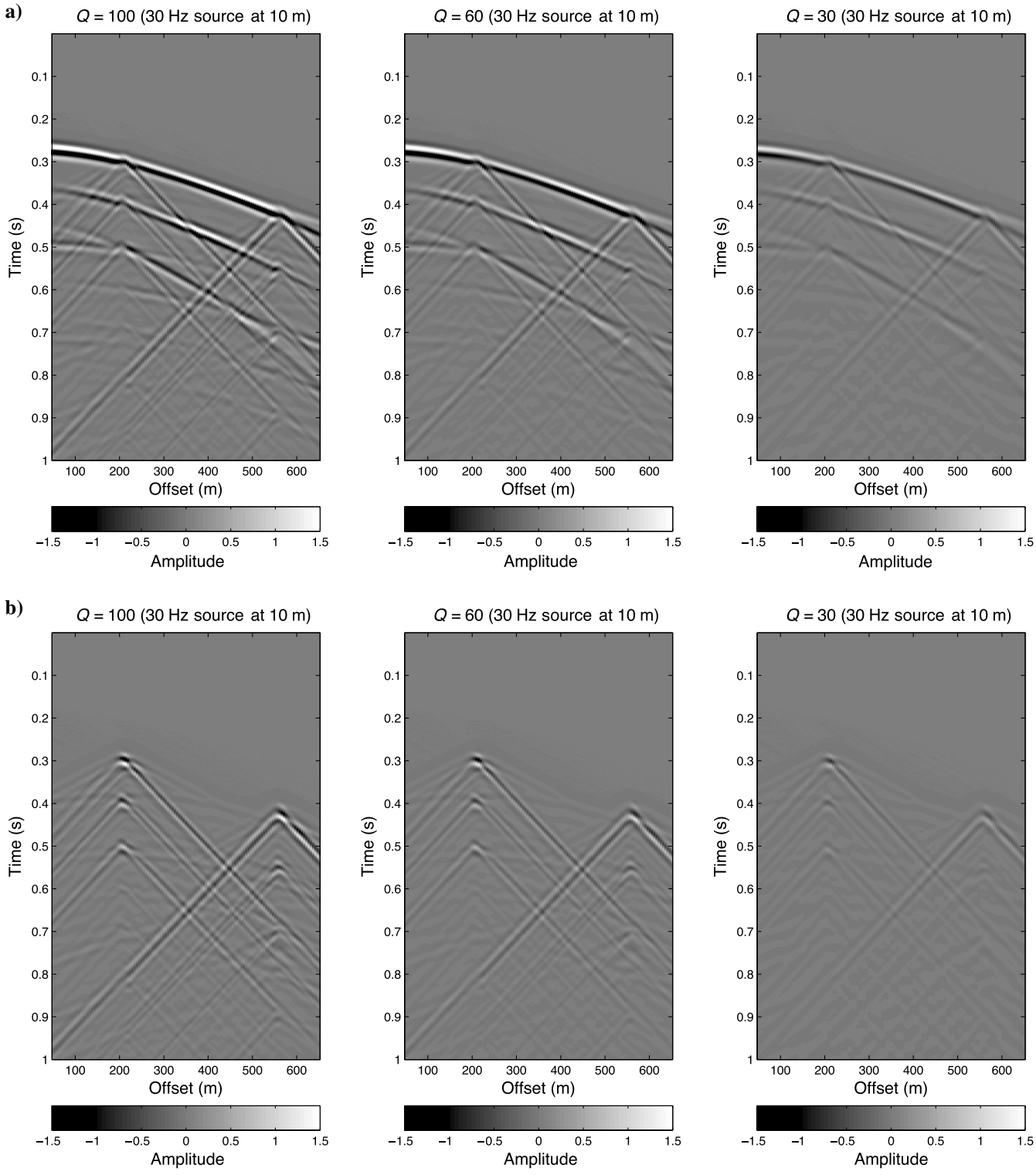

Figure 14. Simulated waveforms (v_z-component) for the scattering model with different attenuation factors in the top layer ($Q = 100$, 60, and 30) from left to right. The source (30 Hz) is located at 10-m depth, and the receivers are located on the surface: (a) the total wavefield simulated using the model with scatterers and (b) the scattered wavefield (i.e., the difference between the total and incident wavefields).

are excited by the near-surface heterogeneities and are independent of the seismic source depth (Figure 10b). The maximum at ~10-m source depth in Figure 10b is most likely related to the constructive/destructive interference between the primary and ghost reflections from the free surface. However, the change in the S/N is very small compared to the other three cases. On the other hand, deploying receivers at depth (Figure 9) can improve the S/N as they sample the weaker energy of the direct and scattered surface waves (Figure 10c and 10d). A recent field data study by Bakulin et al. (2012) agrees with our numerical results and demonstrates the S/N improvement due to deploying the sources and receivers at depth. Bakulin et al. (2012) also look into using dual-sensor data (geophones and hydrophones) to reduce ghost reflections from the free surface to further improve the stacked section.

The effects of scatterers' depth, size, impedance contrast, and attenuation

As discussed in the previous section, the seismic source wavelength and source and receiver depths have great effects on the recorded signal. Nevertheless, the characteristics of near-surface scatterers (e.g., impedance contrast, depth, size, and attenuation factor of the background medium) have similar, if not even greater, effects. These characteristics have direct impact on the phase and amplitude of scattered surface waves and body waves.

Recorded waveforms simulated using models similar to the ones shown in Figure 3 with varying scatterer impedances (Table 2) corresponding to reflection coefficients (0.16, 0.27, and 0.36), depths (15, 30, and 45 m), diameters (10, 20, and 40 m), and attenuation factor Q of the background medium (30, 60, 100, and 200) are shown in Figures 11–14. We show all the figures with the same amplitude scale for ease of comparison. The impedance contrast is calculated as $R_0 = (Z_2 - Z_1)/(Z_2 + Z_1)$, where Z_1 and Z_2 are the impedances (i.e., velocity times density) of the top layer and the scatterers. In all the cases we study in this and remaining sections, we use an explosive point source at 10-m depth as the standard source.

The effects of the scatterer characteristics are demonstrated by showing the total wavefields, which include incident, multiple

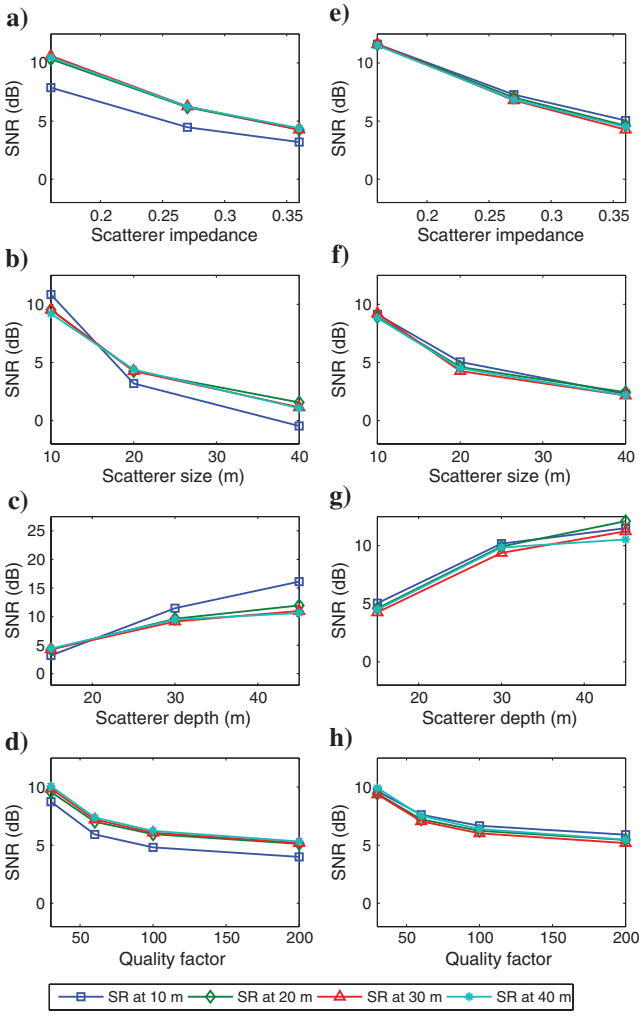

Figure 15. The effects of source depths on the S/N due to characteristics of near-surface heterogeneities (impedance contrast, depth, size, and quality factor) (a-d) including the direct surface waves, and (e-h) with the direct surface waves removed.

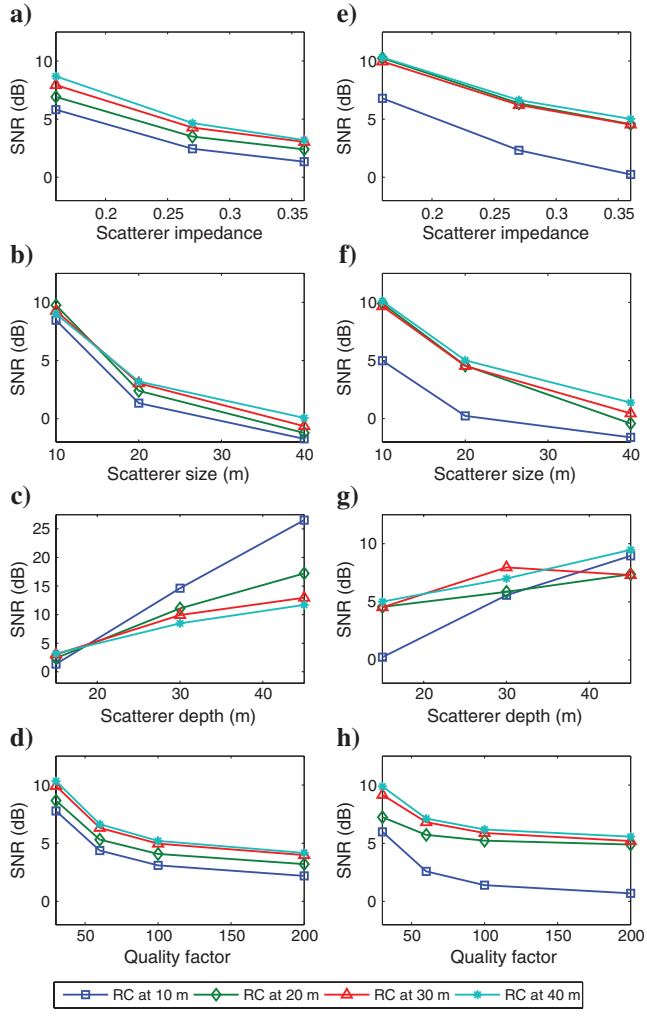

Figure 16. The effects of receiver depths on the S/N due to characteristics of near-surface heterogeneities (impedance contrast, depth, size, and quality factor) (a-d) including the direct surface waves and (e-h) with the direct surface waves removed.

scattering, and mode-converted waves. We quantitatively assess the effects of source and receiver depths and characteristics of near-surface heterogeneities, such as material properties, depths, and sizes, by calculating the S/Ns. The aim is to understand when the scattered waves have significant impact on the quality of the recorded data. As discussed previously, the scattered energy increases with increasing impedance contrast, increasing size of the scatterers relative to the source wavelength, decreasing depth, and increasing attenuation factor of the background medium.

In the first case shown in Figure 11, we vary the impedance contrast by changing the velocity and density of the scatterers, while keeping the properties of the embedding layer constant. The simulations demonstrate that the strength of the scattered energy increases with increasing the impedance contrast of the scatterers. This is explained mathematically by equation 5 in which the right side is equivalent to an elastic source that depends on the material property perturbations.

The frequency of scattered body-to-surface waves depends on the frequency of the total wavefield and the perturbations of the medium parameters. The wavefield scattering amplitude is frequency dependent, and, therefore, the size of the scatterers relative to the wavelength is indeed a controlling factor for the scattered energy. The dominant wavelength of the incident wavefield is

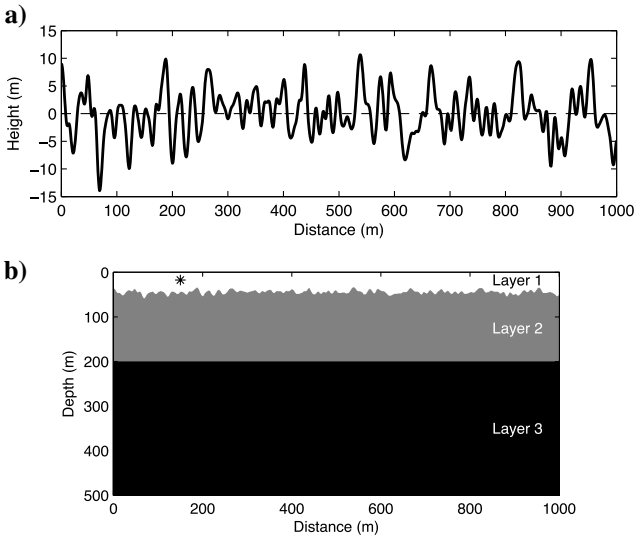

Figure 17. An earth model with near-surface irregular (Gaussian) interface and deeper flat reflector: (a) Gaussian surface profile and (b) the earth model. Material properties are given in Table 3.

Table 3. Material properties (P-wave velocity, S-wave velocity, and density) of the model shown in Figure 17.

Layer no.	V_P (m/s)	V_S (m/s)	Density (kg/m^3)
I	1800	1000	1750
II	3000	1500	2250
III	5000	2250	2750

60 m, and the minimum wavelength is 24 m. We show the simulations for different scatterer sizes in Figure 12: 10-, 20-, and 40-m diameter. Scattered energy depends on the depth of the scatterers. When changing the scatterer size, the top edge of the scatterers is kept at 5-m depth from the free surface and the centers are located at 10, 15, and 25 m, respectively. Thus, the frequency of scattered waves is either low or high depending on whether the size of the scatterers is small or large relative to the wavelength of the incident waves (Figure 12). Similar to increasing the impedance contrast, larger scatterers cause more scattered energy that is lower in frequency compared to small scatterers.

The effects of attenuation are studied by using constant Q models and recalculating some models that were run with no attenuation. We included attenuation only at the top layer of the model shown in Figure 3 with (Q = 100, 60, and 30). The scatterers and the half-space are assumed to be perfectly elastic ($Q = \infty$) materials. The results in Figure 14 demonstrate that the scattered, and also the reflected, wave amplitudes decrease due to attenuation.

The results of different simulations with varying properties are summarized in Figures 15 and 16 as expressed by S/Ns. The S/N increases with decreasing impedance contrast, decreasing size of the scatterers relative to the source wavelength, increasing depth, and decreasing attenuation factor of the background medium. As discussed in the previous section, deeper receivers improve the S/N as they record weaker direct and scattered surface waves, whereas deeper sources improve the S/N only because they excite weaker direct surface waves. The same relationships hold for different impedance contrast (Figures 15a, 16a, and 16e), sizes of the scatterers (Figures 15b, 16b, and 16f), and attenuation factors (Figures 15d, 16d, and 16h). Note, however, that the deeper source has no effect on the scattered body-to-surface waves as indicated by the narrow range of S/N values for different source depths in Figure 15e–15h. These relations hold only when the heterogeneities are shallow (e.g., 15-m depth) and excite significant scattered surface-wave energy. In the case in which the scatterers are close to the free surface, the scattered energy is dominated by body-to-surface-wave scattering (Figure 13). When the scatterers are deeper than one-third of the wavelength (e.g., 20 m), weak or no scattered surface waves are generated and, therefore, there is no S/N improvement due to deploying the receivers below the free surface.

SCATTERING DUE TO BEDROCK TOPOGRAPHY (INTERFACE SCATTERING)

In the previous sections, we showed the examples of scattering from isolated individual scatterers. Bedrock topography (e.g., subsurface irregular interface) can also cause scattering and could have pronounced effects on the quality of recorded waveforms. The irregular interface not only causes time shifts (as assumed by static corrections) but also causes complicated scattering. We model a case when the top of the interface layer is not a plane but irregular.

We consider an earth model with an irregular (Gaussian) surface below a homogeneous surface layer, as shown in Figure 17. The irregular interface is modeled using a set of uncorrelated random numbers drawn from a Gaussian distribution with zero mean and a standard deviation of 15 m (rms height). The generated random numbers (surface) are then correlated by the use of a running average filter with a Gaussian operator that has 5-m correlation length (Ogilvy and Merklinger, 1991). The corresponding material

properties are given in Table 3. An explosive point source at 10-m depth is used with a Ricker wavelet and 30-Hz central frequency. The receivers are located on the surface with 50-m near offset and 5-m space intervals. Simulated waveforms recorded at surface for an irregular interface at 15- and 45-m depths are shown in Figure 18.

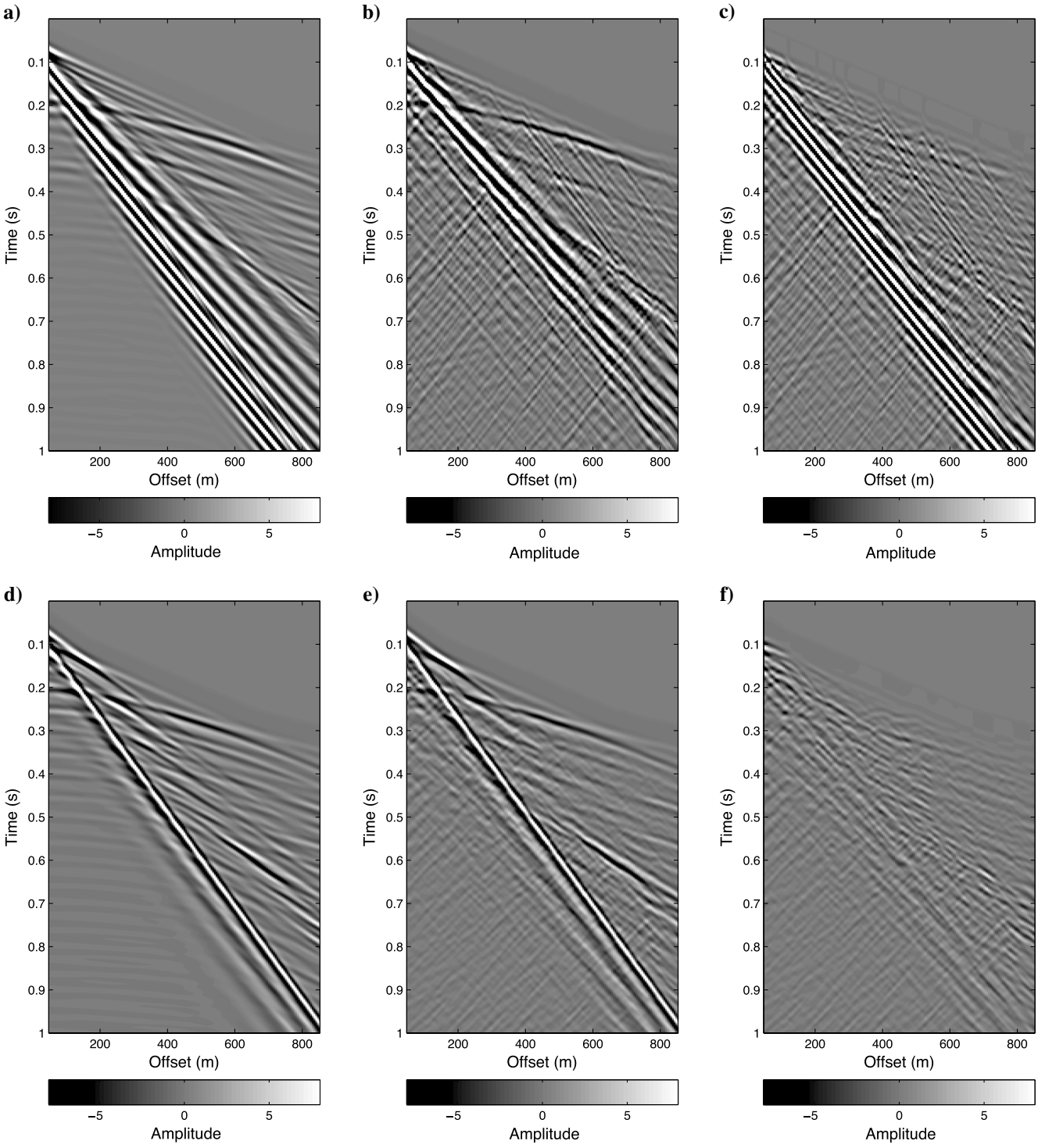

Figure 18. Finite-difference simulations (v_z-component) for the irregular (Gaussian) interface at different depths: (a-c) 15 m, and (d-f) 45 m. The incident wavefield (a and d) simulated using the model with plane shallow interface, (b and e) total wavefield simulated using the model with Gaussian shallow interface, and (c and f) scattered wavefield (i.e., the difference between the total and incident wavefields). Note the strong dispersive character of the surface wave due to the thin layer (a-c). Also, note that the amplitudes of scattered (reflected and refracted) body waves to surface waves decrease rapidly as the interface depth increases. Overall, scattering from the irregular near-surface interface is more complex and exhibits more diffusive-type scattering compared to localized scatterers.

The influence of the irregular interface is clearly demonstrated because it acts as a continuous line of sources that adds to the complexity of the recorded waveforms, compared to the localized scatterers discussed in the previous section. Scattering from irregular interface exhibits diffusive-type scattering compared to individual scattering. The wavelength of Rayleigh waves propagating along the free surface is ($\lambda_R \sim 930$ ms/30 Hz = 31 m). At a 15-m interface depth, we observe a strong surface-wave dispersion due to the thin layer (Figure 18a–18c). Because the surface-wave amplitude at a depth deeper than one-third of the wavelength is very small, scattering and dispersion of direct surface waves are very minimal for the interface at 45-m depth (Figure 18d–18f).

The irregular interface also causes the upgoing reflections and refracted waves to scatter to P- and S-waves. Because the irregular interface is shallow, upgoing body waves and refracted waves, which travel along the irregular interface boundary, scatter to surface waves that can mask the data entirely. The energy of scattered surface waves decreases as the depth of the irregular interface increases, mainly because the interface irregularities act as a source of scattered waves. The scattered energy is dominated by body-to-body waves (i.e., relatively small amplitude) for deep scatterers. However, scattering of reflected and refracted body waves to surface waves (i.e., relatively large amplitude waves) is dominated in the case of the shallow irregular interface.

CONCLUSIONS

In this paper, we present a numerical approach based on the perturbation method and finite-difference forward modeling for simulating the effects of seismic wave scattering from arbitrary-shaped, shallow, subsurface heterogeneities. The scattered wavefield, due to the near-surface scatterers only, is modeled by taking the difference between the incident and total wavefields. We show analytically and numerically that the scatterers act as secondary sources for the scattered elastic wavefield. The numerical results show that scattering of upgoing reflections by the heterogeneities to surface waves can obscure weak primary reflections and contaminate the entire data set. We carried out extensive numerical experiments to study the effects of scattered surface waves on the S/N.

The results show that the scattered energy depends strongly on the properties of the shallow scatterers and increases with increasing impedance contrast, increasing size of the scatterers relative to the incident wavelength, decreasing depth of scatterers, and increasing the attenuation factor of the background medium. Additionally, sources deployed at depths below one-third of the wavelength excite weak surface waves and, therefore, improve the S/N due to the reduced surface-wave scattering. However, source depth does not affect the scattering of reflected body waves. On the other hand, receivers deployed at depth improve the S/N as they record weak surface and scattered body-to-surface waves.

In addition to showing the effects of volume scatterers, we also examine the effects of scattering from a near-surface irregular interface or bedrock topography. Similar to scattering from near-surface inclusions, the energy of scattered body-to-surface waves decreases as the depth of the irregular interface increases. The irregular interface acts as a continuous line of sources for scattered (reflected and refracted) body waves to surface waves, and therefore, the scattered amplitudes decrease as the depth to the interface increases. Compared to scattering from finite scatterers, scattering from an irregular interface exhibits diffusive-type scattering.

The analysis and quantified results help explain the scattering mechanisms and, therefore, could lead to developing new acquisition and processing techniques to reduce the noise and enhance the quality of the subsurface image. For computational efficiencies, we consider only 2D models, but the same method can be applied to 3D modeling. In 3D, however, the computational cost will be much larger, but with current advances in multicore parallel programming and the existence of large clusters, computations with tens of billions of cells are feasible.

ACKNOWLEDGMENTS

We thank Saudi Aramco and ERL founding members for supporting this research. We also thank Saudi Aramco for granting permission to show the field data example used in this paper. X. Campman and three anonymous reviewers provided comments that helped to improve the paper, and we are grateful for their assistance.

APPENDIX A

PERTURBATION OF THE ELASTIC-WAVE EQUATION

The derivation of a wave equation for the scattered wavefield $\mathbf{u}'$ based on the perturbation quantities is obtained by subtracting equation 3 from 1

$$[\rho\ddot{\mathbf{u}} - (\lambda + 2\mu)\nabla(\nabla \cdot \mathbf{u}) + \mu\nabla \times (\nabla \times \mathbf{u})] - [\rho_0\ddot{\mathbf{u}}_0 - (\lambda_0 + 2\mu_0)\nabla(\nabla \cdot \mathbf{u}_0) + \mu_0\nabla \times (\nabla \times \mathbf{u}_0)] = 0, \tag{A-1}$$

by expanding and collecting like terms

$$[\rho\ddot{\mathbf{u}} - \rho_0\ddot{\mathbf{u}}_0] + [-(\lambda + 2\mu)\nabla(\nabla \cdot \mathbf{u}) + (\lambda_0 + 2\mu_0)\nabla(\nabla \cdot \mathbf{u}_0)] + [\mu\nabla \times (\nabla \times \mathbf{u}) - \mu_0\nabla \times (\nabla \times \mathbf{u}_0)] = 0, \tag{A-2}$$

$$[\rho_0\ddot{\mathbf{u}} - \rho_0\ddot{\mathbf{u}}_0 + \rho\ddot{\mathbf{u}} - \rho_0\ddot{\mathbf{u}}] + [-(\lambda_0 + 2\mu_0)\nabla(\nabla \cdot \mathbf{u}) + (\lambda_0 + 2\mu_0)\nabla(\nabla \cdot \mathbf{u}_0) - (\lambda + 2\mu)\nabla(\nabla \cdot \mathbf{u}) + (\lambda_0 + 2\mu_0)\nabla(\nabla \cdot \mathbf{u})] + [\mu_0\nabla \times (\nabla \times \mathbf{u}) - \mu_0\nabla \times (\nabla \times \mathbf{u}_0) + \mu\nabla \times (\nabla \times \mathbf{u}) - \mu_0\nabla \times (\nabla \times \mathbf{u})] = 0, \tag{A-3}$$

$$[\rho_0(\ddot{\mathbf{u}} - \ddot{\mathbf{u}}_0) + (\rho - \rho_0)\ddot{\mathbf{u}}] - [(\lambda_0 + 2\mu_0)\nabla(\nabla \cdot (\mathbf{u}\text{-}\mathbf{u_0})) + ((\lambda - \lambda_0) + 2(\mu - \mu_0))\nabla(\nabla \cdot \mathbf{u})] + [\mu_0\nabla \times (\nabla \times (\mathbf{u} - \mathbf{u}_0)) + (\mu - \mu_0)\nabla \times (\nabla \times \mathbf{u})] = 0, \tag{A-4}$$

substituting equations 2 and 4

$$[\rho_0\ddot{\mathbf{u}}' + \delta\rho\ddot{\mathbf{u}}] - [(\lambda_0 + 2\mu_0)\nabla(\nabla \cdot \mathbf{u}') + (\delta\lambda + 2\delta\mu)\nabla(\nabla \cdot \mathbf{u})] + [\mu_0\nabla \times (\nabla \times \mathbf{u}') + \delta\mu\nabla \times (\nabla \times \mathbf{u})] = 0, \tag{A-5}$$

and rearranging the terms

$$\rho_0 \ddot{\mathbf{u}}' - (\lambda_0 + 2\mu_0)\nabla(\nabla \cdot \mathbf{u}') + \mu_0 \nabla \times (\nabla \times \mathbf{u}') = -[\delta\rho\ddot{\mathbf{u}} - (\delta\lambda + 2\delta\mu)\nabla(\nabla \cdot \mathbf{u}) + \delta\mu\nabla \times (\nabla \times \mathbf{u})]. \quad \text{(A-6)}$$

REFERENCES

Al-Husseini, M. I., J. B. Glover, and B. J. Barley, 1981, Dispersion patterns of the ground roll in eastern Saudi Arabia: Geophysics, **46**, 121–137, doi: 10.1190/1.1441183.

AlMuhaidib, A. M., M. M. Fehler, M. N. Toksöz, and Y. M. Zhang, 2011, Finite difference elastic wave modeling including surface topography: 81st Annual International Meeting, SEG, Expanded Abstracts, 2941–2946.

Appelö, D., and N. A. Petersson, 2009, A stable finite difference method for the elastic wave equation on complex geometries with free surfaces: Communications in Computational Physics, **5**, 84–107.

Bakulin, A., R. Burnstad, M. Jervis, and P. Kelamis, 2012, Evaluating permanent seismic monitoring with shallow buried sensors in a desert environment: 82nd Annual International Meeting, SEG, Expanded Abstracts, doi: 10.1190/segam2012-0951.1.

Beylkin, G., and R. Burridge, 1990, Linearized inverse scattering problems in acoustics and elasticity: Wave Motion, **12**, 15–52, doi: 10.1016/0165-2125(90)90017-X.

Blonk, B., and G. C. Herman, 1996, Removal of scattered surface waves using multicomponent seismic data: Geophysics, **61**, 1483–1488, doi: 10.1190/1.1444073.

Blonk, B., G. C. Herman, and G. G. Drijkoningen, 1995, An elastodynamic inverse scattering method for removing scattered surface waves from field data: Geophysics, **60**, 1897–1905, doi: 10.1190/1.1443921.

Campman, X., and C. D. Riyanti, 2007, Non-linear inversion of scattered seismic surface waves: Geophysical Journal International, **171**, 1118–1125, doi: 10.1111/j.1365-246X.2007.03557.x.

Campman, X. H., G. C. Herman, and E. Muyzert, 2006, Suppressing near-receiver scattered waves from seismic land data: Geophysics, **71**, no. 4, S121–S128, doi: 10.1190/1.2204965.

Campman, X. H., K. van Wijk, J. A. Scales, and G. C. Herman, 2005, Imaging and suppressing near-receiver scattered surface waves: Geophysics, **70**, no. 2, V21–V29, doi: 10.1190/1.1884831.

De Bremaecker, J. C., 1958, Transmission and reflection of Rayleigh waves at corners: Geophysics, **23**, 253–266, doi: 10.1190/1.1438465.

Emmerich, H., and M. Korn, 1987, Incorporation of attenuation into time-domain computations of seismic wave fields: Geophysics, **52**, 1252–1264, doi: 10.1190/1.1442386.

Ernst, F. E., G. C. Herman, and A. Ditzel, 2002, Removal of scattered guided waves from seismic data: Geophysics, **67**, 1240–1248, doi: 10.1190/1.1500386.

Fornberg, B., 1988, The pseudospectral method: Accurate representation of interfaces in elastic wave calculations: Geophysics, **53**, 625–637, doi: 10.1190/1.1442497.

Fuyuki, M., and Y. Matsumoto, 1980, Finite difference analysis of Rayleigh wave scattering at a trench: Bulletin of the Seismological Society of America, **70**, 2051–2069.

Gélis, C., D. Leparoux, J. Virieux, A. Bitri, S. Operto, and G. Grandjean, 2005, Numerical modeling of surface waves over shallow cavities: Journal of Environmental and Engineering Geophysics, **10**, 111–121, doi: 10.2113/JEEG10.2.111.

Graves, R. W., 1996, Simulating seismic wave propagation in 3D elastic media using staggered-grid finite differences: Bulletin of the Seismological Society of America, **86**, 1091–1106.

Greaves, R. J., and T. J. Fulp, 1987, Three-dimensional seismic monitoring of an enhanced oil recovery process: Geophysics, **52**, 1175–1187, doi: 10.1190/1.1442381.

Herman, G. C., P. A. Milligan, Q. Dong, and J. W. Rector, 2000, Analysis and removal of multiply scattered tube waves: Geophysics, **65**, 745–754, doi: 10.1190/1.1444773.

Hestholm, S., and B. Ruud, 1994, 2D finite-difference elastic wave modelling including surface topography: Geophysical Prospecting, **42**, 371–390, doi: 10.1111/j.1365-2478.1994.tb00216.x.

Hudson, J., 1977, Scattered waves in the coda of P: Journal of Geophysics, **43**, 359–374.

Kelly, K., R. Ward, S. Treitel, and R. Alford, 1976, Synthetic seismograms: A finite-difference approach: Geophysics, **41**, 2–27, doi: 10.1190/1.1440605.

Knopoff, L., and A. F. Gangi, 1960, Transmission and reflection of Rayleigh waves by wedges: Geophysics, **25**, 1203–1214, doi: 10.1190/1.1438807.

Komatitsch , D., and R. Martin, 2007, An unsplit convolutional perfectly matched layer improved at grazing incidence for the seismic wave equation: Geophysics, **72**, no. 5, SM155–SM167, doi: 10.1190/1.2757586.

Kristek, J., P. Moczo, and R. J. Archuleta, 2002, Efficient methods to simulate planar free surface in the 3D 4th-order staggered-grid finite-difference schemes: Studia Geophysica et Geodaetica, **46**, 355–381, doi: http://dx.doi.org/10.1023/A:1019866422821.

Levander, A. R., 1988, Fourth-order finite-difference P-SV seismograms: Geophysics, **53**, 1425–1436, doi: 10.1190/1.1442422.

Levander, A. R., 1990, Seismic scattering near the Earth's surface: Pure and Applied Geophysics, **132**, 21–47, doi: 10.1007/BF00874356.

Lumley, D. E., 1995, Seismic time-lapse monitoring of subsurface fluid flow: Ph.D. thesis, Stanford University.

Martin, R., and D. Komatitsch, 2009, An unsplit convolutional perfectly matched layer technique improved at grazing incidence for the viscoelastic wave equation: Geophysical Journal International, **179**, 333–344, doi: 10.1111/j.1365-246X.2009.04278.x.

Moczo, P., J. Kristek, V. Vavryčuk, R. J. Archuleta, and L. Halada, 2002, 3D heterogeneous staggered-grid finite-difference modeling of seismic motion with volume harmonic and arithmetic averaging of elastic moduli and densities: Bulletin of the Seismological Society of America, **92**, 3042–3066, doi: 10.1785/0120010167.

Ogilvy, J. A., and H. M. Merklinger, 1991, Theory of wave scattering from random rough surfaces: Journal of the Acoustical Society of America, **90**, 3382, doi: 10.1121/1.401410.

Ohminato, T., and B. A. Chouet, 1997, A free-surface boundary condition for including 3D topography in the finite-difference method: Bulletin of the Seismological Society of America, **87**, 494–515.

Pullin, N., L. Matthews, and K. Hirsche, 1987, Techniques applied to obtain very high resolution 3-D seismic imaging at an Athabasca tar sands thermal pilot: The Leading Edge, **6**, 10–15, doi: 10.1190/1.1439353.

Riyanti, C. D., and G. C. Herman, 2005, Three-dimensional elastic scattering by near-surface heterogeneities: Geophysical Journal International, **160**, 609–620, doi: 10.1111/j.1365-246X.2005.02492.x.

Robertsson, J. O., 1996, A numerical free-surface condition for elastic/viscoelastic finite-difference modeling in the presence of topography: Geophysics, **61**, 1921–1934, doi: 10.1190/1.1444107.

Robertsson, J. O., and C. H. Chapman, 2000, An efficient method for calculating finite-difference seismograms after model alterations: Geophysics, **65**, 907–918, doi: 10.1190/1.1444787.

Sato, H., M. C. Fehler, and T. Maeda, 2012, Seismic wave propagation and scattering in the heterogeneous earth: Springer.

Tessmer, E., D. Kosloff, and A. Behle, 1992, Elastic wave propagation simulation in the presence of surface topography: Geophysical Journal International, **108**, 621–632, doi: 10.1111/j.1365-246X.1992.tb04641.x.

Virieux, J., 1986, P-SV wave propagation in heterogeneous media: Velocity-stress finite-difference method: Geophysics, **51**, 889–901, doi: 10.1190/1.1442147.

Wu, R., and K. Aki, 1985, Scattering characteristics of elastic waves by an elastic heterogeneity: Geophysics, **50**, 582–595, doi: 10.1190/1.1441934.

Wu, R.-S., 1989, The perturbation method in elastic wave scattering: Pure and Applied Geophysics, **131**, 605–637, doi: 10.1007/BF00876266.

Zhang, W., and X. Chen, 2006, Traction image method for irregular free surface boundaries in finite difference seismic wave simulation: Geophysical Journal International, **167**, 337–353, doi: 10.1111/j.1365-246X.2006.03113.x.

Zhang, W., and Y. Shen, 2010, Unsplit complex frequency-shifted PML implementation using auxiliary differential equations for seismic wave modeling: Geophysics, **75**, no. 4, T141–T154, doi: 10.1190/1.3463431.

Zhang, Y., 2010, Modeling of the effects of wave-induced fluid motion on seismic velocity and attenuation in porous rocks: Ph.D. thesis, Massachusetts Institute of Technology.